Geotechnique
November 2014, Volume 64 Issue 11 Pages 851-864
http://dx.doi.org/10.1680/geot.13.P.125
http://archimer.ifremer.fr/doc/00245/35621/

Mechanical behaviour of gas-charged fine sediments: model formulation and calibration

Sultan Nabil [1, *], Garziglia Sebastien [1, *]

[1] IFREMER, REM GM LES, Plouzane, France.

* Corresponding authors : Nabil Sultan, email address : nabil.sultan@ifremer.fr ;
Sébastien Garziglia, email address : Sebastien.Garziglia@ifremer.fr

Abstract :

Multi-phase fluid conditions encountered in geotechnical and geo-environmental problems have led to the development of models that account for the influence of gas solubility and compressibility on the behaviour of soils of various grain sizes. Yet, no consideration has been given to damages related to the nucleation and growth of gas bubbles in fine-grained soils. The purpose of this paper is to present a Cam Clay based constitutive model extended to incorporate such detrimental effects on gassy soils. This is achieved by deriving an analytical expression relating the preconsolidation pressure to a damage parameter dependent on the gas content. That expression is coupled to a deviatoric yield surface accounting for inherent and stress-induced anisotropy. Comparisons of simulations and experimental results attest that introducing a single additional parameter to a conventional Cam Clay type model allows key behavioural features of gas-charged fine sediments to be reproduced.

Keywords : compressibility, constitutive relations, offshore engineering, shear strength

2 INTRODUCTION

Free gas partially saturating underwater sediments are produced biogenically or thermogenically (Fleischer et al., 2001; Sills and Thomas, 2002). Direct observations in marine sediments have shown the gas phase to be discontinuous forming discrete, isolated bubbles or voids within a continuous water phase (Sills et al., 1991; Anderson et al., 1998; Boudreau et al., 2005). Following Nageswaran (1983), the term ‘gassy soil’ is used to refer to this type of multi-fluid phase conditions and sediment macrostructure. Sparks (1963) and subsequently Nageswaran (1983) argue that the critical water saturation level for the gas phase to be discontinuous is about 0.85. The presence of gas bubbles can have significant effects on the consolidation behaviour and strength properties with gassy soils reacting differently compared to saturated soils to environmental changes in load and temperature (Esrig and Kirby, 1977; Sills and Wheeler, 1992; Grozic et al., 1999; Sills and Gonzalez, 2001; Amaratunga and Grozic, 2009; Puzrin et al., 2011; Sultan et al., 2012; Rebata-Landa and Santamarina, 2012). Accordingly, gas-charging has important consequences for slope stability assessment, waste management and in turn for the planning of on- and off-shore engineering operations (Wheeler et al., 1991; van Kessel and van Kesteren, 2002; Tjelta et al., 2007; Mabrouk and Rowe, 2011). In the following, the effect of free gas on the consolidation and strength properties of fine-grained soils and marine sediments is discussed. This serves as a basis to compare a number of constitutive models that have attempted to predict the behaviour of gassy soils. A new simple constitutive model is then presented to account for the effects of gas exsolution and expansion on the stress-strain response of soils.

3 ON THE BEHAVIOUR OF GASSY FINE-GRAINED SOILS

3.1 The structure of fine-grained, cohesive gassy soils

Observational and theoretical results have pointed out that following gas exsolution (nucleation), bubble growth (gas expansion) may mainly occur in fine-grained soils by compressing and fracturing the saturated matrix or by reopening pre-existing fractures (Boudreau, 2012 and references therein). This can be reconciled with the arguments presented by van Kesteren and van Kessel (2002) concerning the dependence of bubble nucleation and growth on the tensile fracture toughness and undrained shear strength of the soil matrix. Therefore, the main process behind the de-saturation of fine-grained soils is rarely related to expulsion of water from capillary-type pores as described by Van Genuchten type models (van Genuchten 1980) giving a unique relation between the degree of water saturation and the gas and water pressures.

3.2 Undrained unloading of gassy soils

The most detrimental effects of gas on marine soils are encountered during undrained unloading as it may imply gas exsolution and expansion (Hardy and Hemstock, 1963). Because of these two processes, under undrained unloading conditions, changes in volume of gassy soils may occur with pore pressure responses being dramatically different from that of saturated soils (Sobkowicz and Morgenstern, 1984). Sobkowicz and Morgenstern (1984) developed a detailed theoretical model based on a closed-form solution for undrained pore pressure responses to changes in total stress, by applying volume compatibility and considering gas expansion and exsolution.

3.3 Elastic properties

Experimental measurements on gassy, reconstituted silty-clay samples presented by Wheeler and Gardner (1989) clearly showed that the undrained shear modulus, G_u, and the undrained bulk modulus, K_u, both decrease along with the degree of water saturation (S_r). Sultan et al. (2012) noted that the presence of gas has a similar effect on the G_u of natural Gulf of Guinea (GoG) clay samples. Other results of triaxial tests reported by Wheeler et al., (1991) revealed that the normalised Young's modulus measured at an axial strain of 0.25% decreases with increasing the degree of gas saturation.

3.4 Consolidation properties.

Due to the high compressibility of gas bubbles, the application of a load to a fine-grained gassy soil causes volume change even in undrained conditions (Thomas, 1987; Sills et al., 1991). Oedometer results reported by Puzrin et al. (2011) confirm that the saturated clayey matrix and the gas make independent contributions to the overall gassy soil compressibility. Most importantly, the works of Thomas (1987) and Puzrin et al. (2011) both point out that, although the presence of a highly compressible gas phase results in enhanced immediate settlement, total consolidation values may be almost identical for specimens with or without gas. Accordingly, fine-grained gassy soils consolidate along the normal consolidation line (NCL) of their fully saturated equivalent.

3.5 Yield properties

Based on a series of constant rate of strain (CRS) oedometer tests on samples of Lierstranda and Bothkennar clays Lunne et al (2001) emphasised that the preconsolidation pressure (p'_c) tends to decrease when the degree of gas saturation increases. Similar, results from Hight et al. (2002) on Nile delta clay sample led Hight and Leroueil (2003) to ascribe the observed

decreases in p'_c to bubble growth-induced damages to soils structure. They proposed that the degree of damage depends on the initial level of structure. Sultan et al. (2012) furthered this view by defining a damage parameter '*d*' in the form :

$$d = n.(1 - S_r) \qquad \text{[Eq. 1]}$$

where *n* is the porosity. Note that '*d*' is equivalent to the volume fraction of bubbles '*f*' used by Wheeler (1988a).

Experimental data presented in Figure 1 were used by Sultan et al. (2012) to define a relation between p'_c of fine-grained gassy soils and '*d*' in the form:

$$\frac{p'_c}{p'_{c0}} = \exp(-\delta.d) \qquad \text{[Eq. 2]}$$

Where p'_{c0} is the preconsolidation pressure in water-saturated condition and δ a shape parameter found to be equal to 4.3 for GoG clays (Sultan et al., 2012).

3.6 Strength properties

Wheeler (1988a) found that the undrained shear strength (*Su*) of reconstituted silty-clay samples may be increased or decreased by the presence of methane bubbles depending on the specific values of total and effective stresses. He concluded that the effects of gas bubbles on strength properties were most detrimental at low values of effective stress (corresponding to shallow depth below seabed) and high values of total stress (corresponding to deep water location). Wheeler (1988a) also noted that, while the degree of water saturation (S_r) increased during undrained shearing, many gassy samples reached full saturation before failure but their structure remained permanently affected by the earlier presence of the bubbles.

In addition to these triaxial test results, those presented by Lunne et al. (2001), Hight et al. (2002) and Sultan et al. (2012) on natural clays all point out that the gas presence (i) promotes a more contractive response and (ii) significantly reduces the peak shear strength. These authors

have also noted that gas may have the effect of producing a discontinuity in the effective stress path. According to Hight and Leroueil (2003), such a discontinuity (illustrated in Figure 2) arises from a rapid increase in pore pressure, presumably resulting from the collapse of the pores enlarged (damaged) by gas exsolution and expansion.

In the following, the notion of 'enlarged pore' will be referred to as 'gas-formed void', in a similar sense to what Boudreau (2012) interchangeably calls crack, fracture or bubble. Additionally, the processes of gas exsolution and expansion will simply be referred to as 'bubble growth'.

With these specifications in mind, it is worth stressing that, while Lunne et al. (2001) presented results where the different stress paths join the same critical state line (CSL) after the gas-formed voids collapsed, GoG clays reach ultimate conditions on two different CSL (Sultan et al., 2012). In view of the results presented by Le (2008), Sultan et al. (2012) and Hattab et al. (2013) on fully saturated specimens, this is inherent to the sensitivity of GoG clay and to structural damages upon pre-shear consolidation to high stress levels.

4 MODELS ACCOUNTING FOR THE BEHAVIOUR OF FINE-GRAINED GASSY SOILS

Based on the concept that, when soil particles are much smaller than gas-formed voids, the saturated matrix can be treated as a continuum, Wheeler (1988b) proposed the so-called 'large bubble model'. By analysing this continuum model Wheeler (1988a) derived theoretical expressions for the normalised undrained shear strength Su/Su_{sat} (where Su_{sat} is the undrained shear strength in fully saturated condition). In this approach, the saturated matrix was assumed to be a rigid-perfectly plastic von Mises-type material containing empty spherical cavities. Wheeler (1988a) proposed that lower bound values of Su/Su_{sat} can be estimated by ignoring the increase in strength caused by bubble flooding and the work-hardening effect caused by bubble

shrinkage. He added that higher bound values may also be obtained by considering complete flooding of all the gas-formed voids. Various experimental results have been shown by Wheeler et al. (1991) to fit neatly within those theoretical bounds. However, Sultan et al. (2012) recently emphasised that the accuracy of the predictions from the Wheeler's approach tend to decrease inversely with the consolidation stress level achieved after bubble growth.

Pietruszczak and Pande (1996) and Grozic et al. (2005) proposed constitutive models to predict the response of gassy soils under undrained triaxial compression loading. Although these two models differ in complexity, they are both based on the critical state concept and on the idea that, because of its compressibility and solubility, gas only affects the volume change of a soil without damaging its structure. Both of these models predict that the higher the initial gas content, the less significant the total increase in pore pressure during shearing. This in turn leads to predictions that *Su* should increase with increasing gas content.

5 A NEW CONSTITUTIVE MODEL FOR GASSY SOILS/SEDIMENTS

Our proposed constitutive model is based on Cam Clay theory (Roscoe and Burland 1968) with few additions to account for the following key features of fine-grained gassy soils behaviour:

- Bubble growth due to undrained unloading simultaneously reduces the effective stress and the degree of pore water saturation.
- Damage due to bubble growth increase the compressibility and decrease the preconsolidation pressure as well as the shear strength of the initially saturated soil.
- The collapse of gas voids upon shearing may produce a discontinuity in the effective stress path.

The model is based on the uniqueness of the CSL which is recognised as a limitation to accurately reproduce the behaviour of some sensitive clays such as those from the GoG as previously discussed (§ 3.6).

5.1 Model formulation

5.1.1 Isotropic stress states

The formulation is carried out in the specific volume (V)/mean effective stress (p') space based on what Alonso et al. (1990) formulated for unsaturated soils. In this V/p' space, the isotropic behaviour imposes a limiting condition to the formulation of the gassy soils model. Under undrained unloading conditions, the Sobkowicz and Morgenstern (1984) model allows to calculate the change in specific volume, V_d and mean effective stress p'_{int} due to bubble growth (Figure 3). Accordingly, the following identity may be established from Figure 3:

$$V_0 - \lambda.\ln\frac{p'_{c0}}{p'_0} + \kappa.\ln\frac{p'_{c0}}{p'_{\text{int}}} + V_d - \kappa_d.\ln\frac{p'_c}{p'_{\text{int}}} - V_c = V_0 - \lambda.\ln\frac{p'_c}{p'_0} \qquad \text{[Eq. 3]}$$

The Cam Clay parameters κ and λ are, respectively, the intact swelling coefficient and the compression index. p'_c is given by equation 2 and κ_d is a damaged swelling coefficient accounting for the effect of bubble growth. The quantity V_c is seen as a collapse required to reach the NCL. It can be calculated from :

$$V_c = \ln\left(\frac{p'_{c0}}{p'_{\text{int}}}\right).(\kappa - \kappa_d) + V_d + \delta.d.(\kappa_d - \lambda) \qquad \text{[Eq. 4]}$$

Given the lack of detailed experimental investigations concerning κ_d, two limit cases can be considered following undrained unloading and consequent bubble growth:

Case 1: κ_d increases and the compression curve reaches the NCL at the yield locus (Puzrin et al., 2011) defined by equation 2. In this case, V_c is equal to 0 and, according to equations 2 and 4, κ_d can be calculated as follows :

$$\kappa_d = \frac{-\kappa\ln\left(\frac{p'_{c0}}{p'_{\text{int}}}\right) - V_d + \lambda.\delta.d}{-\ln\left(\frac{p'_{c0}}{p'_{\text{int}}}\right) + \delta.d} \qquad \text{[Eq. 5]}$$

Case 2: κ_d remains constant ($\kappa = \kappa_d$) and a collapse V_c takes place at the yield locus defined by equation 2. The compression curve reaches the NCL after the collapse of gas-formed voids. The collapse can be calculated from equation 4 with κ equal to κ_d.

5.1.2 Triaxial stress states

On extending the model to triaxial states of stress and strain, the deviatoric stress q is introduced. The model adopted to simulate the saturated (limit) condition is that developed by Banerjee et al. (1985) to account for inherent and stress-induced anisotropy of natural clays. It is based on the modified Cam Clay model where, in addition to the isotropic hardening law, an additional stress tensor is introduced in the yield curve expression. Under axisymetric loading (radial stresses are equal – condition of triaxial test), the Banerjee et al. (1985) yield curve is given by the following equation:

$$q = \frac{2}{3} p' \frac{q_0}{p'_0} \pm \sqrt{M^2 \left(p' p'_0 - p'^2 \right) + \frac{1}{9} \frac{p'}{p'_0} q_0^2} \qquad \text{[Eq. 6]}$$

where q and p' are respectively the deviatoric and mean effective stress invariants, M is the slope of the CSL, and q_0 and p'_0 are the projection of the additional stress tensor in the q:p' space (Figure 4-a). q_0 is related to p'_0 through the following equation:

$$q_0 = -3p'_0 \frac{K_0 - 1}{2K_0 + 1} \qquad \text{[Eq. 7]}$$

where K_0 is the coefficient of earth pressure at rest; q_0 and p'_0 are the maximum stresses a saturated soil has previously been loaded to. For a soil with a purely isotropic stress history, (q_0 equals to zero) the yield curve of the Banerjee et al. model is similar to that of the modified Cam Clay model.

The use of the Banerjee et al. (1985) yield curve, as presented in Figure 4, is justified by the initial anisotropy of most natural sediments. The isotropic preconsolidation pressure p'_c of the damaged gassy sediment can be calculated from p'_0 according to the following equation:

$$\frac{p'_c}{p'_0} = \frac{M^2 \exp(-\delta.d)^2 \left(4K_0^2 + 4K_0 + 1\right) + (K_0 - 1)^2}{\exp(-\delta.d)\left[(2K_0 - 2)^2 + M^2\left(2K_0^2 + 1\right)^2\right]} \qquad \text{[Eq. 8]}$$

The isotropic preconsolidation pressure p'_{c0} of the saturated sediment is given by the following equation:

$$\frac{p'_{c0}}{p'_0} = \frac{4M^2 K_0 [K_0 + 1] + M^2 + K_0^2 - 2K_0 + 1}{4\left[K_0^2 + 1 + M^2 - 4K_0 + M^2 K_0^2 + M^2 K_0\right]} \qquad \text{[Eq. 9]}$$

5.1.3 Hardening law, consistency conditions and flow rule

Similarly to the modified Cam Clay model, the hardening law here adopted is isotropic. It gives dp'_{c0} as a function of the volumetric plastic strain increment $d\varepsilon_v^p$ according to the following equation:

$$dp'_{c0} = \frac{1 + e_0}{\lambda - \kappa}.p'_{c0}.d\varepsilon_v^p \qquad \text{[Eq. 10]}$$

The shrinkage of the yield curve is also induced by bubble growth. As previously discussed, it leads to a decrease of p'_c and therefore to a decrease of p'_0 and q_0.

The increment of plastic volumetric strain $d\varepsilon_v^p$ can be calculated by applying the consistency condition, defined by $dF_1 = 0$ if $\frac{q}{p'} > \frac{q\left[p'_0 + \frac{q_0^2}{p'_0}\frac{1}{9M^2}\right]}{p'_0 + \frac{q_0^2}{p'_0}\frac{1}{9M^2}}$ and $dF_2 = 0$ if $\frac{q}{p'} < \frac{q\left[p'_0 + \frac{q_0^2}{p'_0}\frac{1}{9M^2}\right]}{p'_0 + \frac{q_0^2}{p'_0}\frac{1}{9M^2}}$

Where

$$F_1 = q - \frac{2}{3}p'\frac{q_0}{p'_0} - \sqrt{M^2\left(p'\,p'_0 - p'^2\right) + \frac{1}{9}\frac{p'}{p'_0}q_0^2} \qquad \text{[Eq. 11]}$$

and

$$F_2 = q - \frac{2}{3} p' \frac{q_0}{p'_0} + \sqrt{M^2 \left(p' \, p'_0 - p'^2 \right) + \frac{1}{9} \frac{p'}{p'_0} q_0^2} \qquad \text{[Eq. 12]}$$

The two consistency conditions $dF_1 = 0$ and $dF_2 = 0$ are given by the following equation:

$$dF_{1-2} = \left(\frac{\partial F_{1-2}}{\partial p'} \right) dp' + \left(\frac{\partial F_{1-2}}{\partial q} \right) dq + \left(\frac{\partial F_{1-2}}{\partial d} \right) dd + \left(\frac{\partial F_{1-2}}{\partial p'_0} . \frac{\partial p'_0}{\partial p'_{c0}} \right) dp'_{c0} \qquad \text{[Eq. 13]}$$

Where $\frac{\partial p'_0}{\partial p'_{c0}}$ can be determined from equation 2.

The partial differential terms in equation 13 are given in Table 1 and Table 2. Therefore $d\varepsilon_v^p$ can be calculated by combining equations 10 and 13.

In most constitutive models for saturated soils, the plastic potential only depends on the stress inclination *q/p'* (Roscoe and Burland 1968; Wong and Mitchell 1975 and Nova and Wood 1979). For this reason, the flow rule can be investigated by plotting the direction of the plastic strain ratio $d\varepsilon_v^p / d\varepsilon_s^p$ as a function of the stress ratio *q/p'*. Here, the following expression proposed by Lagioia et al. (1996) is used:

$$\frac{d\varepsilon_v^p}{d\varepsilon_s^p} = \mu \left(M_c - \frac{q}{p'} \right) \left(\frac{\alpha M_c}{\frac{q}{p'}} + 1 \right) \qquad \text{[Eq. 14]}$$

where M_c corresponds to the value of *q/p'* at which $d\varepsilon_v^p / d\varepsilon_s^p$ is equal to 0.

5.2 Parameters of the model and their determination

In total, ten parameters (κ, κ_d, G, λ, M, μ, α, M_c, δ, K_0) are introduced in the proposed model. They can be determined as follows:

(a) κ, G, λ, M are common Cam Clay parameters which can be determined in a common fashion;

(b) κ_d can be determined from isotropic compression tests after gas exsolution. Alternatively, κ_d can be taken equal to κ or derived from equation 5 for the two limit cases presented in § 5.1.1.

(c) μ, α and *Mc* which define the flow rule are calculated by using the $d\varepsilon_v^p / d\varepsilon_s^p$ - *q/p'* curve obtained from a drained triaxial test on a fully saturated sample.

(d) δ which governs the shape of the yield locus in the *p'-d* space can be derived from at least two isotropic compression tests at two different damage levels (or two different initial S_r).

(e) For the yield curve the K_0 parameter corresponds to the coefficient of earth pressure at rest.

The determination of the degree of water saturation, undrained volume change and pore water pressure due to the gas compressibility and solubility are calculated using the Sobkowicz and Morgenstern model which requires input soil and water compressibilities as well as the Henry's coefficient.

5.3 Model performance

The aim of this section is to show the capability of the model to simulate different drained and undrained stress paths. The following set of model parameters is used for the different simulations:

Flow rule: $\mu = 1.2$, $\alpha = 0.001$, $M_c = 1.75$

Yield locus in the *d*/*p'* plane: $\delta = 4.3$

Banerjee yield curve: $K_0 = 0.6$

The gas saturating the medium is carbon dioxide whose Henry's coefficient of solubility equals to 0.86.

In addition, the void ratio at 1 kPa (e_0) was taken equal to 5.1 while the initial total stress was taken equal to 10 MPa with a p'_{c0} equal to 0.1 MPa.

5.3.1 Case 1: Drained isotropic loading

Four samples are unloaded undrained from 10 MPa to 4 different lower effective stresses. Upon undrained unloading the initially normally consolidated samples become over-consolidated (Figure 5). The 4 samples are characterised by 4 different effective stresses, void ratios and degrees of water saturation before compression (Figure 5). In Figure 5, , the 4 compression curves follow different damaged swelling coefficients κ_d to converge towards the NCL at 4 different mean effective stresses *p'*.

– In Figure 6, the 4 compression curves follow the same swelling coefficients κ before converging towards the NCL after a volumetric collapse V_c proportional to the initial S_r at 4 different mean effective stresses *p'*. Figure 5 and Figure 6 illustrate the way the two different possibilities concerning κ_d ($V_c = 0$ or $\kappa_d = \kappa$) can be considered in the proposed model.

5.3.2 Case 2: Drained triaxial tests at different initial degrees of water saturation – $V_c=0$

The 3 stress paths considered for this case are presented in Figure 7-a. Two of the 3 samples are first unloaded undrained to cause bubble growth. Following the consequent decreases in *p'* and S_r, the 2 gassy samples as well as the saturated one are submitted to a drained triaxial stress path with a typical *dq/dp'*=3. Figure 7-b shows that the peak shear strength of over-consolidated sediments depend strongly on the size of the yield curve and increases with S_r. The increase of κ_d due to bubble growth is illustrated in Figure 7-c & -d as causing increased compressibility.

5.3.3 Case 3: Undrained triaxial tests at different initial degrees of water saturation - $\kappa_d=\kappa$

The 4 stress paths of this case are presented in Figure 8-a where 3 of the 4 samples are unloaded undrained before shearing. Figure 8-a also shows the yield curve of the saturated sediment (dashed curve). Using $\kappa_d=\kappa$ in the calculation allows to simulate experimentally observed

discontinuities in the stress paths. Each discontinuity corresponding to a sudden increase in pore pressure depends on the damage level '*d*'. The second important observation that can be drawn from Figure 8-a is that the slope of the stress path in the plastic domain changes once S_r becomes equal to 1 (this can be seen on only one stress path, second from the right, presented in Figure 8-a).

The simulation results in terms of deviatoric stress/ shear strain are presented in Figure 8-b where the maximum deviatoric stress increases with S_r. The simulation results are also presented in terms of volumetric strain/ mean effective stress (Figure 8-c) and volumetric strain/deviatoric strain diagram (Figure 8-d) to show that the sediment becomes incompressible when S_r reaches 1 (Figure 8-c & -d).

5.3.4 Case 4: Undrained triaxial tests at different initial degrees of water saturation – V_c = 0

The 4 stress paths followed for this case calculation are presented in Figure 9-a. As previously, 3 of the 4 samples were unloaded undrained before shearing. Figure 9-a also presents the yield curves of the 4 samples (dashed curves). By contrast with the saturated sample, the 3 gassy ones follow inclined stress paths in the elastic domain. The use of $V_c = 0$ in the simulation prevents the sudden increase in pore pressure during shearing and therefore the discontinuity in the stress paths. Once again, the change in slope of the stress path in the plastic domain (for the second test from the right) corresponds to the limit where S_r becomes equal to 1 (Figure 9-a). The simulation results in terms of deviatoric stress/ shear strain are presented in Figure 9-b where the maximum deviatoric stress increases with S_r. The simulation results are also presented in terms of volumetric strain/ mean effective stress (Figure 9-c) and volumetric strain/deviatoric strain diagram (Figure 9-d).

5.4 The Wheeler (1988a) model compared to the proposed one

Although the Wheeler's (1988a) model is not adapted to predict *Su* values when sediments follow complex stress paths before shearing, it was shown to correctly predict *Su* when shearing occurs immediately after bubble growth (Sultan et al., 2012). In order to compare and analyse the two models' sensitivity to their respective input parameters, 28 numerical simulations were carried out by considering stress paths where sediments are directly sheared after bubble growth. The response of sediments of varying properties to different initial total and effective stresses were thus tested (Table 3).

Figure 10 presents five examples (first five in Table 3) of numerical simulations of CIU tests at different initial S_r in a deviatoric stress/mean effective stress diagram where *Su* is calculated from the deviatoric stress at yield q_y ($Su=q_y/2$). Three key features are noticeable in this figure: the stress path inclination in the elastic domain, the discontinuity in the stress path and, the excess pore pressures build-up during plastic shearing when the sediments become water fully saturated (S_r=1).

Simulation results in Figure 11-a present the theoretical lower bounds of *Su* using the Wheeler's (1988a) model and show *Su* to be more sensitive to *d* for high values of p'_{c0} / Su_{sat}. The 28 numerical simulations detailed in Table 3 are presented in Figure 11-b in terms of Su / Su_{sat} as a function of *d*. The Su / Su_{sat} values obtained with the present model are much less sensitive to the value of p'_{c0} / Su_{sat} when compared to the Wheeler's model. However, Su / Su_{sat} depends strongly on the δ parameter so that, for similar values of p'_{c0} / Su_{sat} and *d*, Su / Su_{sat} decreases strongly with increasing δ. Another important observation can be drawn from Figure 11-b where, for the same p'_{c0} / Su_{sat} and the same δ, Su / Su_{sat} decreases significantly with the increase of the κ values. This last observation was expected since the stress path in a Cam Clay-type model depends strongly on κ and λ. The comparison between 5 series of model

predictions shows that the Wheeler's model generally overestimates the degradation in *Su* for a given damage parameter *d*. This is also an expected result since the curves shown in Figure 11 are predicted from the lower bound expression of Su / Su_{sat} proposed by Wheeler (1988a).

5.5 Comparison of model simulations with experimental results

5.5.1 Tests on Nile Delta clay

Hight et al (2002) presented results of CIU tests on Nile Delta clay in which gas exsolution and expansion resulted from stress relief inherent to core sample recovery: two samples, BH10 and BH6A come from 32.35 m and 45.0 m depth, respectively. Before shearing, the two samples were isotropically consolidated to their in situ stress conditions. Hight et al. (2002) have not reported any in situ values of S_r but estimated that just before shearing, the samples had S_r ranging from 0.85 and 0.95.

The isotropic stress paths applied in the numerical simulations before shearing were chosen in order to fit with i) the initial mean effective stress and ii) the elastic limits that can be easily defined from the changes in slope of the effective stress paths. Although this implies that simulations have no predictive significance, comparison of modelling results with experimental data provides insight into the four phases characterising the stress path of Nile Delta clay gassy samples as shown in Figure 12:

- Phase 1: shearing induces slight changes in mean effective stress in the elastic region (due to gas compressibility). This initial phase is well described by the modelling results.

- Phase 2: the collapse of gas-formed voids at yielding induces an important progressive increase in pore pressure under a negligible increase in shear stress. Increases in pore pressure are function of the initial gas-formed voids or S_r. This second phase is well described by the proposed model but the pore pressure increase is simulated as a sudden process rather than a progressive one

- Phase 3: the compression and dissolution of remaining gas bubbles cause a progressive increase in S_r along with a decrease in compressibility (or increase in pore pressure).
- Phase 4: after the complete collapse and disappearance of the gas bubbles, the sediment behaves as a saturated one with an important increase in pore pressure during shearing.

5.5.2 Tests on Lierstranda clay

By conducting a series of CAUc tests on Lierstranda clay with various initial amounts of gas dissolved in the pore water (Figure 13-a), Lunne et al., (2001) evaluated the detrimental effects of stress relief due to deepwater sampling. In the Lunne et al. (2001) tests, The amount of gas initially dissolved in the water (η) was adjusted in the laboratory before the samples were unloaded undrained and then sheared but the change in S_r due to gas exsolution was not measured. Modelling results presented in Figure 13-b show the four phases commented in the above paragraph for the Hight et al. (2002) tests going from elastic shearing to the complete collapse of gas bubbles.

Figure 14 illustrates the ability of the model to fit the experimental stress-strain curves and the decrease in peak deviatoric stress with S_r. However, it is important to mention that predicting the post-peak softening presented in Figure 13-a and Figure 14-a is beyond the capability of the present model. Indeed, the softening of a slightly over-consolidated (OCR < 2) or normally consolidated sediment cannot be simulated without accounting for initial strength sensitivity and/or subsequent degradation of the structure during shearing.

5.5.3 Tests on GoG plastic clay

Sultan et al. (2012) reported results of CIU tests on natural GoG clay samples made gassy by undrained unloading after saturation with carbonated water. The minimum S_r measured before shearing the samples A, B, C and D (in Figure 15-a) were respectively equal to 0.95, 0.93, 0.91 and 0.91. Tests results revealed that damages due to bubble growth have affected the

compressibility, preconsolidation pressure and peak shear strength of those structured sediments (Sultan et al., 2012). Bubble growth might have also contributed to the change in CSL as illustrated in Figure 15-a. Nevertheless, we cannot ignore that this change has been shown (Le et al., 2008) to be also related to destructuration by isotropic compression before shearing. The GoG plastic clays (plasticity index between 90 and 120) are composed of small size elementary clay particles (a few micrometers) assembled in much larger aggregates. The high effective friction angles (exceeding 40°) characterising the GoG natural clays (see for instance Le et al., 2008) may be explained by their microstructure but also by a sand-like behaviour of the clay aggregates.

Therefore, simulating the 4 tests presented in Figure 15-a with the Cam Clay type model presented in this paper is only possible by considering two different values of M: equal to 0.8 for tests D and A and equal to 0.65 for tests B and C. The use of two different M, for the same initial sediment, suggests the presence of two different critical states.

Other parameters used for the simulation of CIU tests were derived from Sultan et al. (2012) and are as follow:

Compressibility: λ=1.0, κ=0.1 and κ_d calculated from equation 5 ($V_c=0$).

Flow rule: μ = 1.2, α = 0.45, Mc = 1.75

Yield locus in the d/p' plane: δ = 4.3

Yield surface: K_0 = 1.0 and therefore q_0 in equation 7 is equal to 0.

Void ratio at 1 kPa (e_0) = 7.7.

The simulation results in Figure 15-b show the two last phases (phases 3 and 4 in § 5.5.1) previously commented for the Hight et al. (2002) tests.

Simulations in Figure 15-b reproduce the observed peak strengths and effective stresses for the four tests (Figure 15-a). The use of $V_c=0$ in the simulation of the GoG clays prevents the advent of discontinuities in the stress path as observed by Lunne et al. (2001) and Hight et al. (2002).

6 CONCLUSION

A Cam Clay based constitutive model was extended to reproduce features of fine-grained gassy sediments behaviour not previously captured by existing models. In the light of experimental results, an analytical expression was derived to relate the preconsolidation pressure to a damage parameter inherent to the growth of gas bubbles. This expression was coupled to an anisotropic yield surface with the addition of a damaged swelling coefficient. The model outlined in this paper was able to fairly reproduce published results of triaxial tests under different loading conditions. Accordingly, the following features of behaviour observed experimentally were reproduced:

- Upon undrained unloading, bubble growth causes important decreases in effective stress and degree of water saturation.
- By reducing the preconsolidation pressure, damage due to bubble growth induces the contraction of the yield surface.
- The onset of yielding may be marked by the collapse of gas-formed voids and an associated significant and sudden increase in pore pressure.
- Owing to the compressibility and solubility of gas, the degree of water saturation increases upon shearing so that fully saturated conditions may be reached before failure.
- By contracting the size of the yield surface and therefore the pore pressure response, damage due to the growth of gas bubble imply that fine-grained gassy sediments reach ultimate conditions at lower shear stresses than their fully saturated equivalent.

ACKNOWLEDGMENT

The authors are thankful for fruitful discussions with Alain Puech. Funding support from the French CITEPH program (http://gep-france.com/citeph/) is also greatly appreciated.

NOTATION

d damage parameter

$d\varepsilon_v^p$ volumetric plastic strain increment

$d\varepsilon_s^p$ deviatoric plastic strain increment

e void ratio

e_0 initial void ratio

G shear modulus

G_u undrained shear modulus

K bulk modulus

K_0 coefficient of earth pressure at rest

K_u undrained bulk modulus

M critical stress ratio

M_c flow rule parameter at which the plastic strains ratio is equal to 0

n porosity

p' mean effective stress

p'_0 maximum mean effective stress supported by the sediment

p'_c preconsolidation pressure

p'_{c0} preconsolidation pressure of the water-saturated soils

p'_{int} effective stress after undrained unloading

q deviatoric stress

q_0 maximum deviatoric stress supported by the sediment

q_y deviator stress at yield

S_r degree of water saturation

Su undrained shear strength

V specific volume

V_c collapse in terms of specific volume at yield

V_d swelling in terms of specific volume after undrained unloading

α first flow rule parameter

δ shape parameter relating the preconsolidation pressure to the damage parameter

η degree of dissolved gas

ε_a axial strain

ε_s deviatoric strain

ε_v volumetric strain

κ swelling coefficient

κ_d damaged swelling coefficient

λ compression index

REFERENCES

Alonso, E. E., Gens, A. & Josa, A. (1990). A constitutive model for partially saturated soils. *Géotechnique*, **40**, 405-430.

Amaratunga, A. & Grozic, J. L. H. (2009). On the undrained unloading behaviour of gassy sands. *Canadian Geotechnical Journal*, **46,** 1267-1276.

Anderson, A. L., Abegg, F., Hawkins, J. A., Duncan, M. E. & Lyons, A. P. (1998). Bubble populations and acoustic interaction with the gassy floor of Eckernforde Bay. *Continental Shelf Research*, **18,** 1807-1838.

Banerjee, P. K., Stipho, A. S. & Yousif, N. B. (1985). A Theoretical and experimental investigation of the behaviour of anisotropically consolidated clay. *Developments in Soil Mechanics and Foundation Engineering*-2 (Elsevier Applied Science Publishers), 1-41.

Barden, L. & Sides,G. R. (1970). Engineering behaviour and structure of compacted clay. *Proceedings ASCE*, *96* (SM4), 1171-1200.

Boudreau, B. R. (2012). The physics of bubbles in surficial, soft, cohesive sediments. *Marine and Petroleum Geology*, **38,** 1-18.

Boudreau, B. P., Algar, C., Johnson, B. D., Croudace, I., Reed, A., Furukawa, Y., Dorgan, K. M., Jumars, P. A., Grader, A. S. & Gardiner, B. S. (2005). Bubble growth and rise in soft sediments. *Geology*, **33,** 517-520.

Esrig, M. I. & Kirby, R. C. (1977). Implications of gas content for predicting stability of submarine slopes. *Marine Geotechnology*, **2,** 81-100.

Fleischer, P., Orsi, T. H., Richardson, M. D. & Anderson, A. L. (2001). Distribution of free gas in marine sediments: a global overview. *Geo-Marine Letters*, **21,** 103-122.

Grozic, J. L., Robertson, P. K. & Morgenstern, N. R. (1999). The behavior of loose gassy sand. *Canadian Geotechnical Journal*, **36,** 482-492.

Grozic, J. L. H., Nadim, F. & Kvalstad, T. J. (2005). On the undrained shear strength of gassy clays. *Computers and Geotechnics*, **32,** 483-490.

Hardy, R. M. & Hemstock, R. A. (1963). Shearing strength characteristics of Athabasca oil sands. In *Volume Research Council of Alberta*, Information Series 45, 109-122.

Hattab, M., Hammad, T., Fleareau, J. M. & Hicher, P. Y. (2013). Behaviour of a sensitive marine sediment: microstructural investigation. *Géotechnique*, **63,** 71-84.

Hight, D. W. & Leroueil, S. (2003). Characterisation of soils for engineering purposes. In *Characterisation and engineering properties of natural soils* (eds T. S Tan, K. K. Phoon, D. W. Hight and S. Leroueil), pp. 255–362. Lisse, the Netherlands: Balkema.

Hight, D. W., Hamza, M. M. & El Sayed, A. S. (2002). Engineering characterization of the Nile Delta clays. In *Coastal geotechnical engineering in practice* (eds A. Nakase and T. Tsuchida), pp. 149–162. Lisse, the Netherlands: Swets & Zeitlinger.

Lagioia, R., Puzrin, A. M. & Potts, D. M. (1996). A new versatile expression for yield and plastic potential surfaces. *Computers and Geotechnics*, **19,** 171-191.

Le, M., Nauroy, J., De Gennaro, V., Delage, P., Flavigny, E., Thanh, N., Colliat, J.L., Puech, A. & Meunier, J. (2008). Characterization of soft deepwater West Africa clays : Shansep testing is not recommended for sensitive structured clays. *Proceedings of the Offshore Technology Conference*, Houston, TX, OTC 19193.

Lunne, T., Berre, T., Stranvik, S., Andersen, K. H. & Tjelta, T. I. (2001). Deepwater sample disturbance due to stress relief. *Proceedings of the OTRC 2001 international conference*, Houston, TX, pp. 64–85.

Mabrouk, A.,Rowe, R.K. (2011). Effect of gassy sand lenses on a deep excavation in a clayey soil. Engineering Geology, **122,** 292–302.

Nageswaran, S. (1983). Effect of gas bubbles on the sea bed behaviour. *D. Phil. Thesis*, Oxford University.

Nova, R. & Wood, D. M. (1979). Constitutive model for sand in triaxial compression. *International Journal for Numerical and Analytical Methods in Geomechanics*, **3,** 255-278.

Pietruszczak, S. & Pande, G. N. (1996). Constitutive relations for partially saturated soils containing gas inclusions. *Journal of Geotechnical Engineering-Asce,* **122,** 50-59.

Puzrin, A. M., Tront, J., Schmid, A. & Hugues, J. B. (2011). Engineered use of microbial gas production to decrease primary consolidation settlement in clayey soils. *Géotechnique,* **61,** 785-794.

Rebata-Landa, V. & Santamarina, J. C. (2012). Mechanical Effects of Biogenic Nitrogen Gas Bubbles in Soils. *Journal of Geotechnical and Geoenvironmental Engineering,* **138,** 128-137.

Roscoe, K. H. & Burland, J. B. (1968). On the generalised stress–strain behaviour of wet clay. In *Engineering plasticity*, pp. 535–609. Cambridge, UK: Cambridge University Press.

Sills, G. C. & Gonzalez, R. (2001). Consolidation of naturally gassy soft soil. *Geotechnique,* **51,** 629-639.

Sills, G. C. & Thomas, S. D. (2002). Pore pressure in soil containing gas. Edited by Di Maio C., Hueckel T., Loret B. *Chemo-Mechanical Coupling in Clays; From nano-scale to engineering applications*, 211-222.

Sills, G. C. & Wheeler, S. J. (1992). The significance of gas for offshore operations. *Continental Shelf Research,* **12,** 1239-&.

Sills, G. C., Wheeler, S. J., Thomas, S. D. & Gardner, T. N. 1991. Behaviour of offshore soils containing gas-bubbles. *Geotechnique,* 41**,** 227-241.

Sobkowicz, J. C. & Morgenstern, N. R. (1984). The undrained equilibrium behavior of gassy sediments. *Canadian Geotechnical Journal*, **21,** 439-448.

Sparks, A. D. W. (1963). Theoretical considerations of stress equations for partly saturated soils. In *Proceedings of the 3rd African conference on soil mechanics and foundation engineering*, Salisbury, Rhodesia, 1, 215-218.

Sultan, N., De Gennaro, V. & Puech, A. (2012). Mechanical behaviour of gas-charged marine plastic sediments. *Géotechnique*, **62**, 751-766.

Thomas, S.D. 1987. The consolidation behaviour of gassy soil. D.Phil. Thesis, Oxford University.

Tjelta, T.I., Svanø, G., Strout, J.M., Forsberg, C.F., Johansen, H. & Planke, S. (2007). Shallow gas and its multiple impact on a North Sea production platform. Proceedings of the 6th Int. Offshore Site Investigation and Geotechnics Conf., 11-13 Sept., London, 205-220.

Van Genuchten, M. Th. (1980). A closed-form equation for predicting the hydraulic conductivity of unsaturated soils. *Soil Sci. Soc. Am. J.*, 44, 892–898.

Van Kessel, T.; van Kesteren, W.G.M. (2002) Gas production and transport in artificial sludge depots; Waste Management., **22**, 19-28.

Van Kesteren W., Van Kessel, T. 2002. Gas bubble nucleation and growth in cohesive sediments. Edited by Winterwerp, J.C., Kranenburg, C. Fine sediment dynamics in the marine environment. Proc Marine Science 5. Elsevier, Amsterdam, 329 -341.

Wheeler, S. J. (1988a). The undrained shear-strength of soils containing large gas-bubbles. *Géotechnique,* **38,** 399-413.

Wheeler, S. J. (1988b). A conceptual-model for soils containing large gas-bubbles. *Géotechnique,* **38,** 389-397.

Wheeler, S. J. & Gardner, T. N. (1989). Elastic-moduli of soils containing large gas-bubbles. *Géotechnique,* **39,** 333-342.

Wheeler, S. J., Sills, G. C., Sham, W.M., Duffy, S.M. & Boden, D.G. (1991). The influence of shallow gas on the geotechnical properties of fine-grained sediments. *Journal of the Society for Underwater Technology*, **17(3)**, 11-16.

Wong, P. K. K. & Mitchell, R. J. (1975). Yielding and plastic-flow of sensitive cemented clay. *Géotechnique,* **25,** 763-782.

TABLE CAPTIONS

Table 1. Differential terms associated with F_1 used in equation 13.

Table 2. Differential terms associated with F_2 used in equation 13.

Table 3. Summary of 28 numerical simulations carried out for different initial test conditions.

FIGURE CAPTIONS

Figure 1. Yield loci in the *d* (damage parameter)/*p'*(mean effective stress) plane.

Figure 2. Schematic effect of gas exsolution on effective stress path in triaxial compression (modified from Hight and Leroueil, 2003).

Figure 3. Compression curve for damaged sediments after undrained unloading. The mean effective stress p'_{int} and the swelling V_d are generated after the undrained unloading path and are calculated from the Sobkowicz and Morgenstern (1984) model.

Figure 4. a) Yield curve in the deviatoric stress- mean effective stress diagram (from Banerjee et al., 1985) and b) yield locus in the *d*/*p'* diagram. The damaged isotropic preconsolidation pressure (p'_c) decreases with the increase of the δ parameter.

Figure 5. Undrained unloading followed by isotropic drained loading with $V_c=0$. Void ratio- mean effective stress relationships.

Figure 6. Undrained unloading followed by isotropic drained loading with $\kappa_d=\kappa$. Void ratio- mean effective stress relationships.

Figure 7. Numerical simulations of 3 drained triaxial tests at 3 different initial degrees of water saturation plotted on a) deviatoric stress/mean effective stress diagram, b) deviatoric stress/deviatoric strain diagram, c) volumetric strain/ mean effective stress diagram and d) volumetric strain/deviatoric strain diagram. The three samples are highly over-consolidated (OCR > 2).

Figure 8. Numerical simulations of 4 undrained triaxial tests at 4 different initial degrees of water saturation plotted on a) deviatoric stress/mean effective stress diagram, b) deviatoric stress/deviatoric strain diagram , c) volumetric strain/ mean effective stress diagram (the plotted values correspond to S_r) and d) volumetric strain/deviatoric strain diagram. The four samples are normally consolidated or slightly over-consolidated (OCR < 2).

Figure 9. Numerical simulations of 4 undrained triaxial tests at 4 different initial degrees of water saturation plotted on a) deviatoric stress/mean effective stress diagram, b) deviatoric stress/deviatoric strain diagram, c) volumetric strain/ mean effective stress diagram (the plotted values correspond to S_r) and d) volumetric strain/deviatoric strain diagram. The four samples are normally consolidated or slightly over-consolidated (OCR < 2).

Figure 10. Example of numerical simulations of five undrained triaxial tests at different initial degrees of water saturation plotted on deviatoric stress/mean effective stress diagram (first five in Table 3). The undrained shear strength *Su* is calculated from q_y ($Su=q_y/2$).

Figure 11. a) Prediction of Su / Su_{sat} as a function of *d* using the Wheeler's (1988a) lower bound model (dashed lines) and the present developed model. b) Su / Su_{sat} as a function of *d* for the test conditions presented in Table 3.

Figure 12. Results of CIU triaxial tests on Nile Delta clay (Hight et al., 2002) in terms of effective stress paths. Bold curves correspond to numerical simulation results (the plotted values correspond to S_r).

Figure 13. Results of CAU_C triaxial tests on Lierstranda clay with different degrees of dissolved gas η (Lunne et al., 2001). Effective stress paths a) experimental results, b) modelling.

Figure 14. Results of CAU_C triaxial tests on Lierstranda clay with different degrees of dissolved gas (Lunne et al., 2001). Stress-strain curves a) experimental results, b) modelling.

Figure 15. Results of triaxial tests on gassy GoG clays with different initial degrees of water saturation (Sultan et al., 2012). Effective stress paths a) experimental results, b) modelling. The sudden decrease observed in the C curve corresponds to an accidental unloading during shearing.

$\frac{\partial \rightarrow}{\partial \downarrow}$	F_1
p'	$\frac{2(K_0-1)}{2K_0+1} - \frac{0.5}{\sqrt{M^2\left(p'\,p'_0\exp(-\delta d) - p'^2\right) + p'\frac{p'_0}{\exp(-\delta d)}\frac{(K_0-1)^2}{(2K_0+1)^2}}}\left[M^2\left(p'_0\exp(-\delta d) - 2p'\right) + \frac{p'_0}{\exp(-\delta d)}\frac{(K_0-1)^2}{(2K_0+1)^2}\right]$
q	1
p'_0	$\frac{-0.5}{\sqrt{M^2\left(p'\,p'_0\exp(-\delta d) - p'^2\right) + p'\frac{p'_0}{\exp(-\delta d)}\frac{(K_0-1)^2}{(2K_0+1)^2}}}\left[M^2 p'\exp(-\delta d) + \frac{p'}{\exp(-\delta d)}\frac{(K_0-1)^2}{(2K_0+1)^2}\right]$
d	$\frac{-0.5}{\sqrt{M^2\left(p'\,p'_0\exp(-\delta d) - p'^2\right) + p'\frac{p'_0}{\exp(-\delta d)}\frac{(K_0-1)^2}{(2K_0+1)^2}}}\left[-M^2 p'\,p'_0\,\delta\exp(-\delta d) + \frac{p'\,p'_0}{\exp(-\delta d)}\frac{(K_0-1)^2}{(2K_0+1)^2}\delta\right]$

Table 1. Differential terms associated with F_1 used in equation 13.

$\frac{\partial \rightarrow}{\partial \downarrow}$	F_2
p'	$\frac{2(K_0-1)}{2K_0+1}+\frac{0.5}{\sqrt{M^2\left(p'\,p'_0\exp(-\delta d)-p'^2\right)+p'\frac{p'_0}{\exp(-\delta d)}\frac{(K_0-1)^2}{(2K_0+1)^2}}}\left[M^2\left(p'_0\exp(-\delta d)-2p'\right)+\frac{p'_0}{\exp(-\delta d)}\frac{(K_0-1)^2}{(2K_0+1)^2}\right]$
q	1
p'_0	$\frac{0.5}{\sqrt{M^2\left(p'\,p'_0\exp(-\delta d)-p'^2\right)+p'\frac{p'_0}{\exp(-\delta d)}\frac{(K_0-1)^2}{(2K_0+1)^2}}}\left[M^2p'\exp(-\delta d)+\frac{p'}{\exp(-\delta d)}\frac{(K_0-1)^2}{(2K_0+1)^2}\right]$
d	$\frac{0.5}{\sqrt{M^2\left(p'\,p'_0\exp(-\delta d)-p'^2\right)+p'\frac{p'_0}{\exp(-\delta d)}\frac{(K_0-1)^2}{(2K_0+1)^2}}}\left[-M^2p'\,p'_0\,\delta\exp(-\delta d)+\frac{p'\,p'_0}{\exp(-\delta d)}\frac{(K_0-1)^2}{(2K_0+1)^2}\delta\right]$

Table 2. Differential terms associated with F_2 used in equation 13.

q_y	Su	S_r	n	d	Su/Su_{sat}	M	δ	$\Delta\sigma$	σ_{ini}	K_0	λ	κ	p'_{c0}/Su_{sat}
53.300	26.650	1.000	0.730	0.000	1.000	1	4.3	0	10000	1	0.5	0.05	3.732
50.530	25.265	0.992	0.731	0.006	0.948	1	4.3	-100	10000	1	0.5	0.05	3.732
43.366	21.683	0.957	0.738	0.032	0.814	1	4.3	-500	10000	1	0.5	0.05	3.732
32.350	16.175	0.912	0.747	0.066	0.607	1	4.3	-1000	10000	1	0.5	0.05	3.732
28.480	14.240	0.893	0.751	0.080	0.534	1	4.3	-1200	10000	1	0.5	0.05	3.732
72.200	36.100	1.000	0.730	0.000	1.000	1.35	4.3	0	10000	1	0.5	0.05	2.765
68.700	34.350	0.992	0.731	0.006	0.952	1.35	4.3	-100	10000	1	0.5	0.05	2.765
58.220	29.110	0.957	0.738	0.032	0.806	1.35	4.3	-500	10000	1	0.5	0.05	2.765
44.240	22.120	0.912	0.747	0.066	0.613	1.35	4.3	-1000	10000	1	0.5	0.05	2.765
39.300	19.650	0.893	0.751	0.080	0.544	1.35	4.3	-1200	10000	1	0.5	0.05	2.765
26.400	13.200	1.000	0.730	0.000	1.000	0.5	4.3	0	10000	1	0.5	0.05	7.464
25.180	12.590	0.992	0.731	0.006	0.954	0.5	4.3	-100	10000	1	0.5	0.05	7.464
21.300	10.650	0.957	0.738	0.032	0.807	0.5	4.3	-500	10000	1	0.5	0.05	7.464
15.780	7.890	0.912	0.747	0.066	0.598	0.5	4.3	-1000	10000	1	0.5	0.05	7.464
13.930	6.965	0.893	0.751	0.080	0.528	0.5	4.3	-1200	10000	1	0.5	0.05	7.464
26.400	13.200	1.000	0.730	0.000	1.000	0.5	2.15	0	10000	1	0.5	0.05	7.464
25.200	12.600	0.992	0.731	0.006	0.955	0.5	2.15	-100	10000	1	0.5	0.05	7.464
22.280	11.140	0.957	0.738	0.032	0.844	0.5	2.15	-500	10000	1	0.5	0.05	7.464
19.360	9.680	0.912	0.747	0.066	0.733	0.5	2.15	-1000	10000	1	0.5	0.05	7.464
26.480	13.240	1.000	0.730	0.000	1.000	0.5	5	0	10000	1	0.5	0.05	7.464
25.180	12.590	0.992	0.731	0.006	0.951	0.5	5	-100	10000	1	0.5	0.05	7.464
21.080	10.540	0.957	0.738	0.032	0.796	0.5	5	-500	10000	1	0.5	0.05	7.464
14.520	7.260	0.912	0.747	0.066	0.548	0.5	5	-1000	10000	1	0.5	0.05	7.464
12.360	6.180	0.893	0.751	0.080	0.467	0.5	5	-1200	10000	1	0.5	0.05	7.464
70.020	35.010	1.000	0.759	0.000	1.000	1	4.3	0	10000	1	0.4	0.2	2.828
68.260	34.130	0.992	0.761	0.006	0.975	1	4.3	-100	10000	1	0.4	0.2	2.828
54.460	27.230	0.958	0.767	0.032	0.778	1	4.3	-500	10000	1	0.4	0.2	2.828
32.080	16.040	0.913	0.776	0.067	0.458	1	4.3	-1000	10000	1	0.4	0.2	2.828

Table 3. Summary of 28 numerical simulations carried out for different initial test conditions.

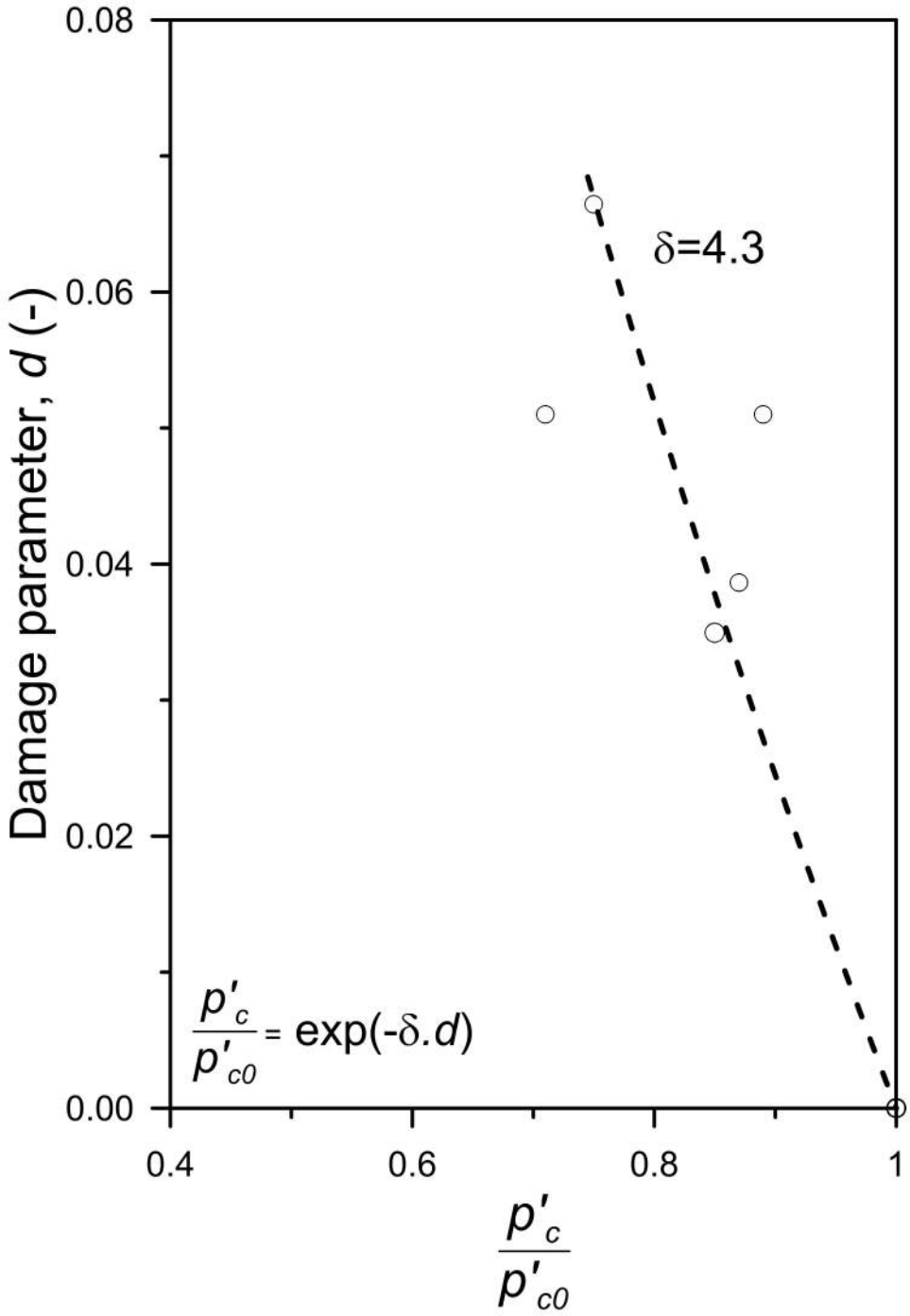
0.08
0.06
0.04
0.02
0.00
Damage parameter, d (-)
δ=4.3
p'c / p'c0 = exp(-δ.d)
0.4
0.6
0.8
1
p'c / p'c0

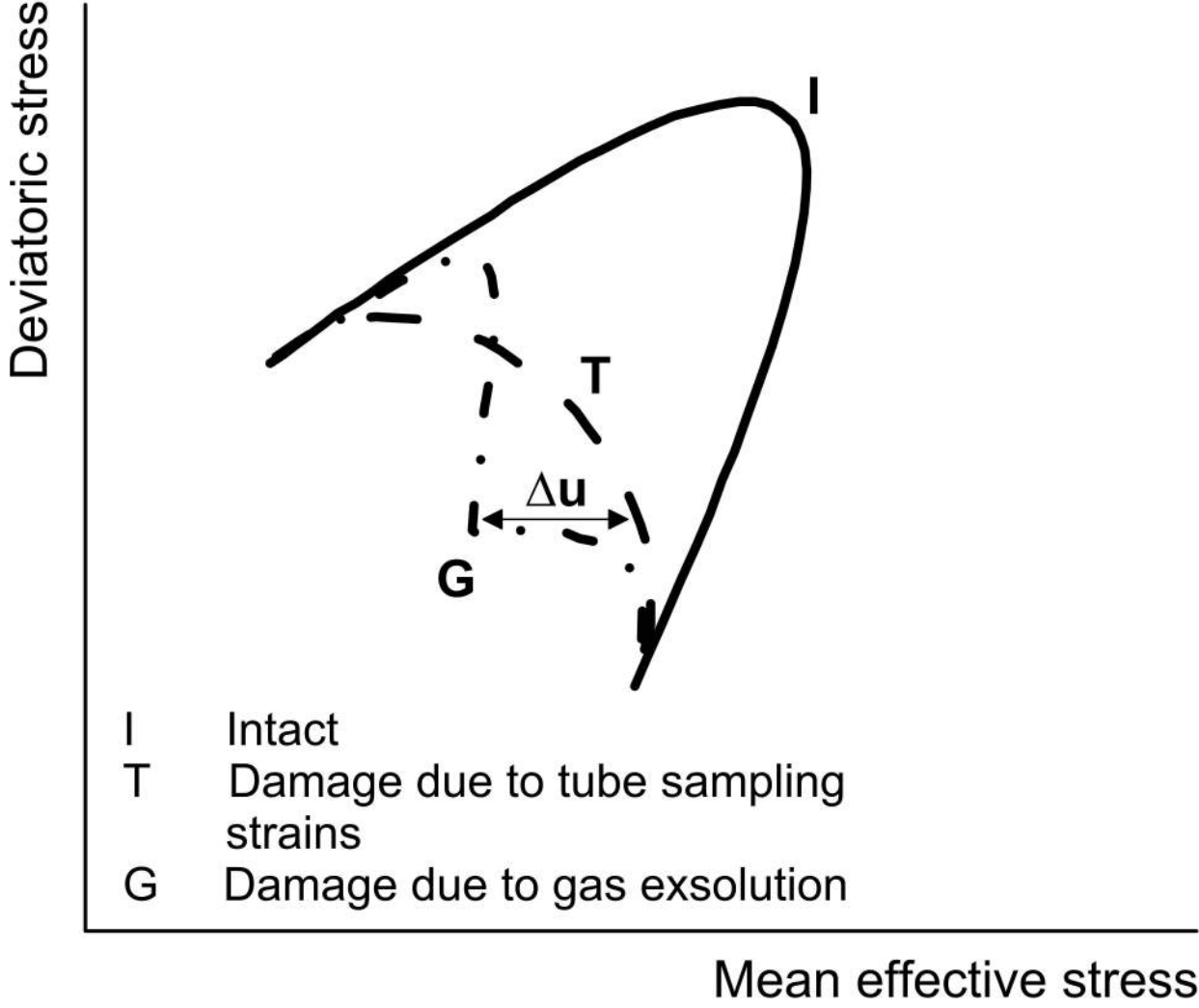
Deviatoric stress
I
T
Δu
G
I Intact
T Damage due to tube sampling strains
G Damage due to gas exsolution
Mean effective stress

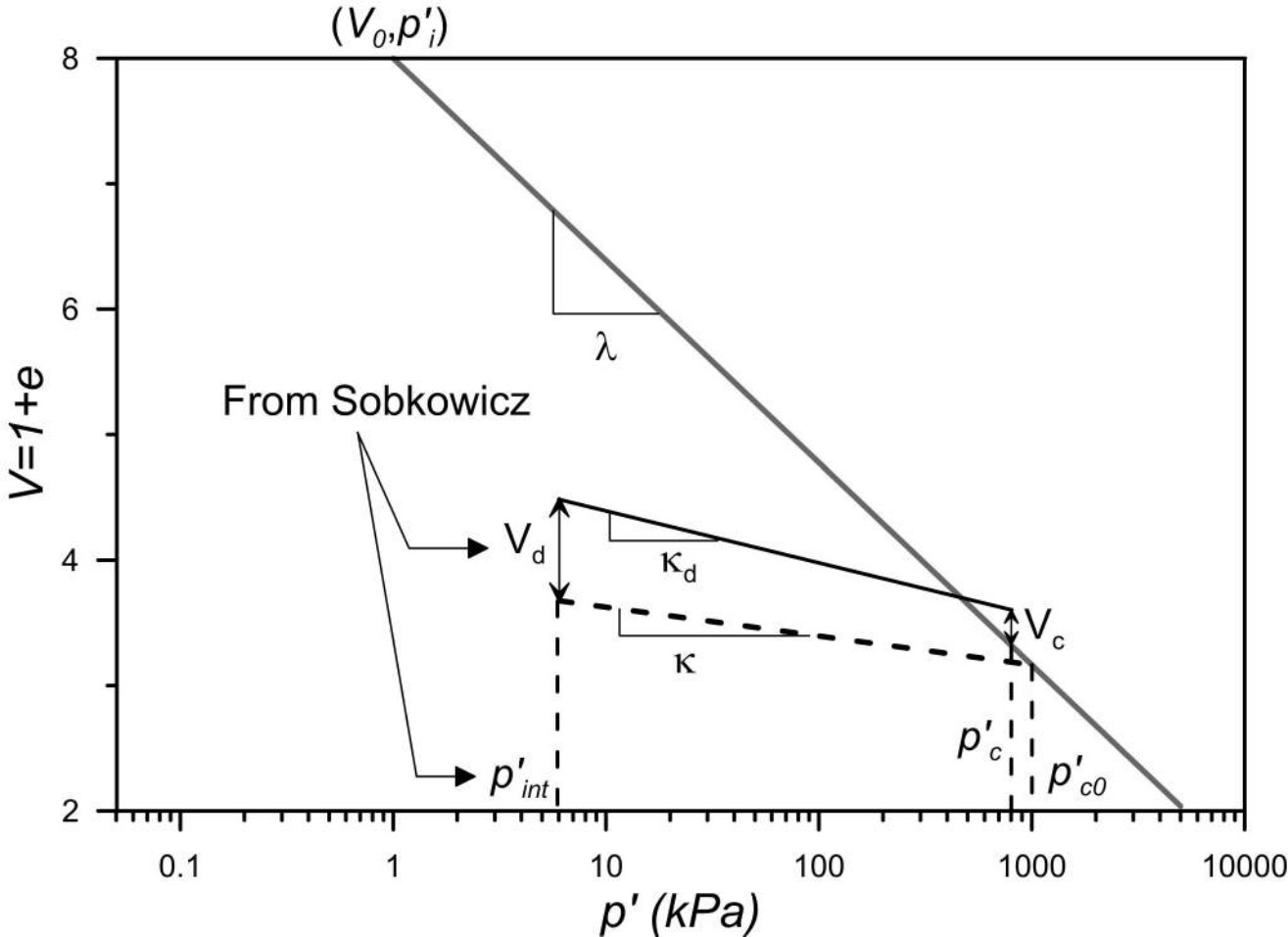
(V_0,p'_i)
8
6
4
2
$V=1+e$
λ
From Sobkowicz
V_d
κ_d
V_c
κ
p'_{int}
p'_c
p'_{c0}
0.1
1
10
100
1000
10000
p' (kPa)

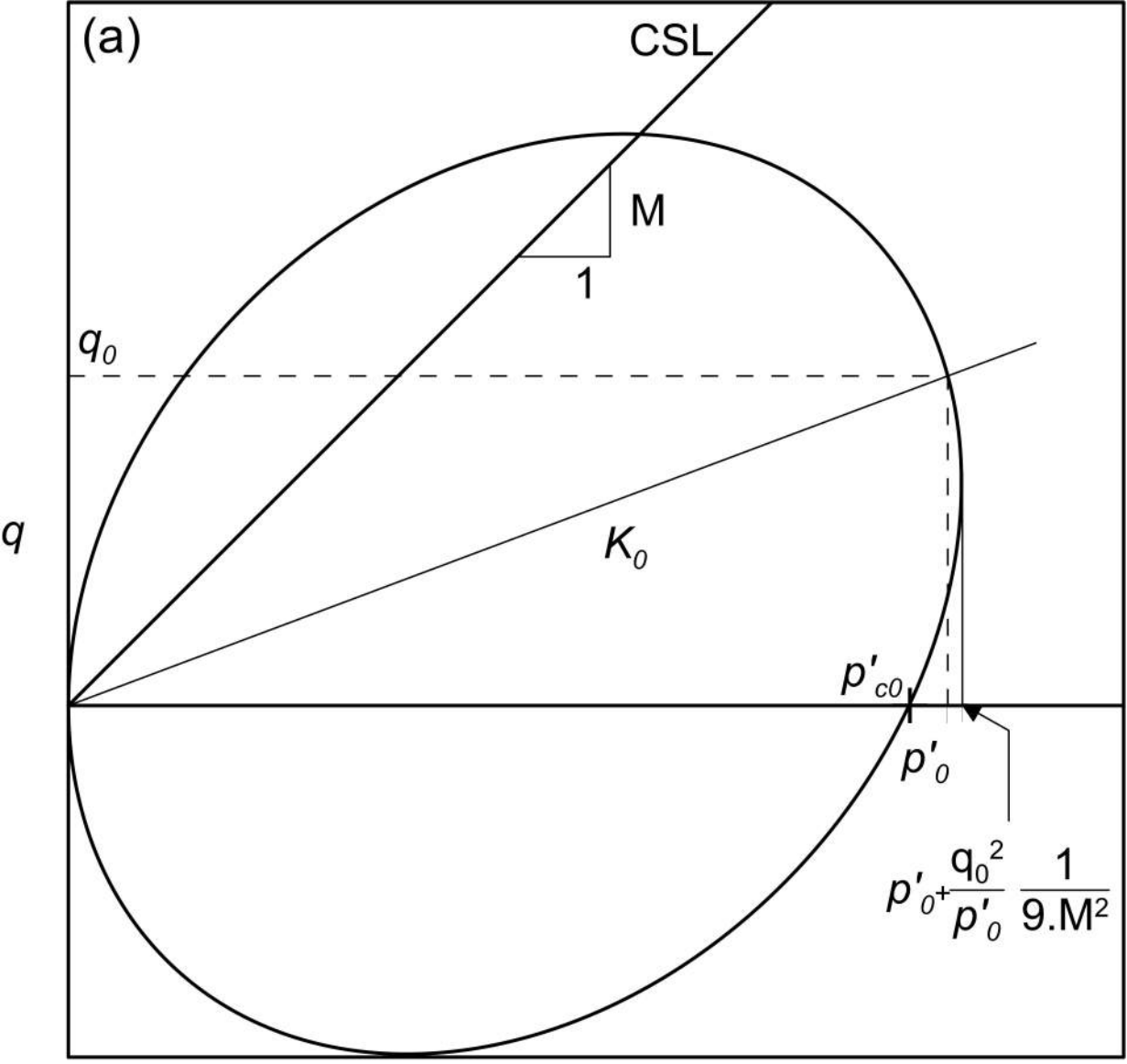
(a)
CSL
M
1
q_0
q
K_0
p'_{c0}
p'_0
$p'_0+\frac{q_0^2}{p'_0}\frac{1}{9.M^2}$

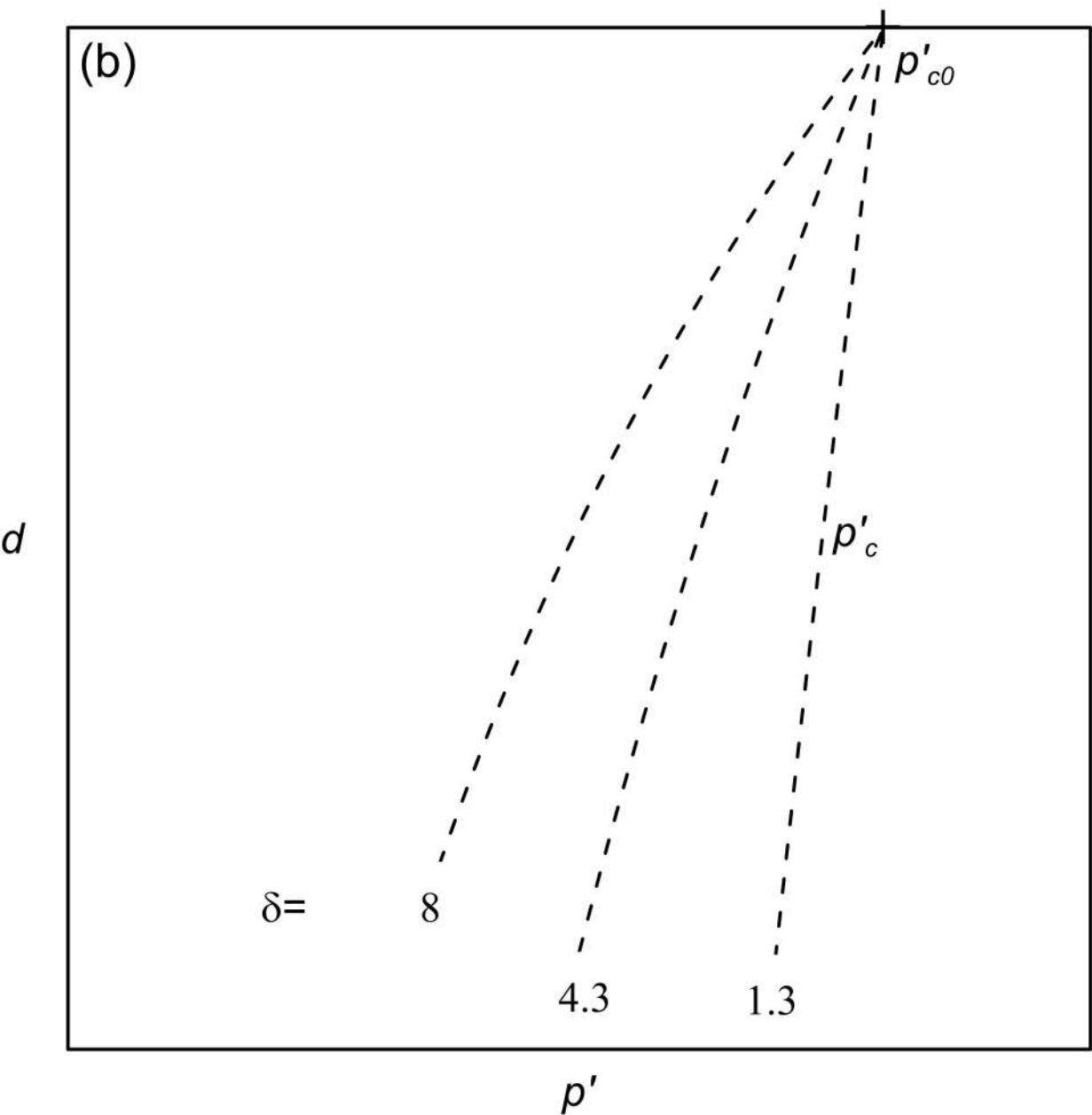
(b)
p'_{c0}
p'_c
d
δ=
8
4.3
1.3
p'

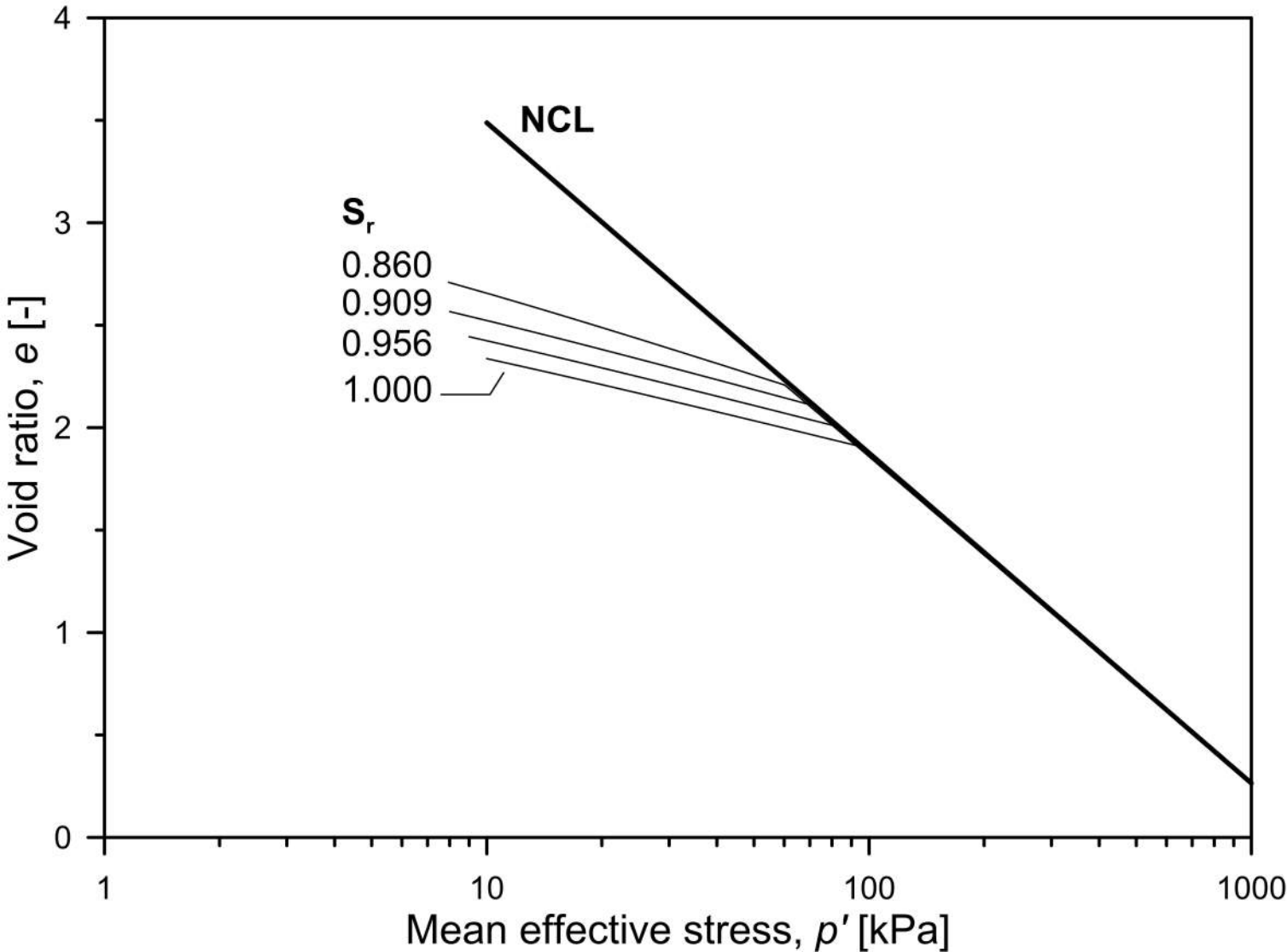
NCL
S_r
0.860
0.909
0.956
1.000
Void ratio, e [-]
Mean effective stress, p' [kPa]
0
1
2
3
4
1
10
100
1000

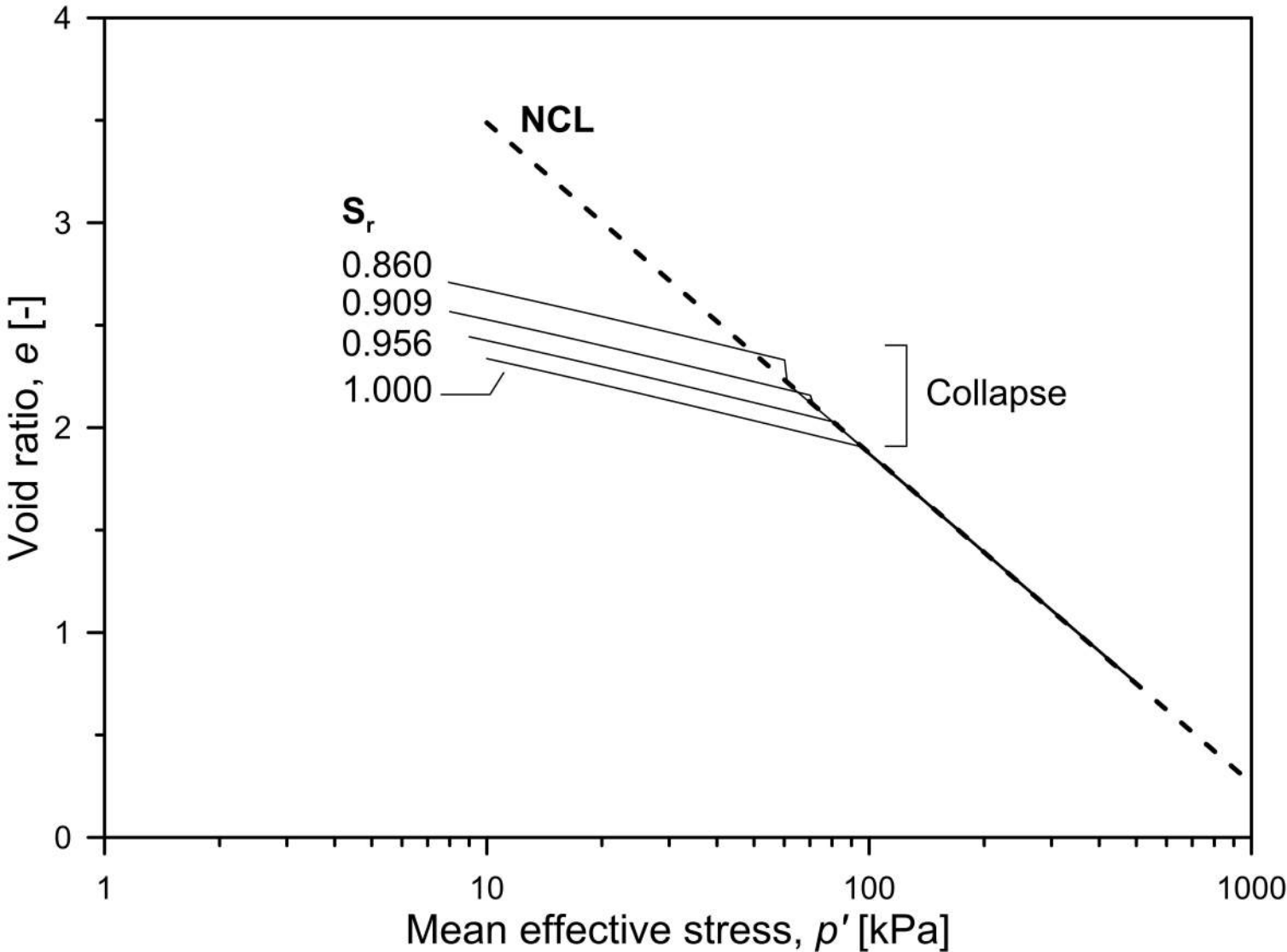
NCL
S_r
0.860
0.909
0.956
1.000
Collapse
Void ratio, e [-]
Mean effective stress, p′ [kPa]
0
1
2
3
4
1
10
100
1000

(a)

1

1.35

Stress paths

Yield curves of S_r=1

Deviatoric stress, q [kPa]

120

80

40

0

0

40

80

120

(b)

S_r = 1

0.956

0.909

120

80

40

0

0

4

8

12

16

20

(c)

0.909

0.956

S_r = 1

Compressibility is function of κ_d

Volumetric strain, ε_v [%]

0.0

2.0

4.0

6.0

8.0

0

40

80

120

Mean effective stress, p' [kPa]

(d)

0.909

0.956

S_r = 1

0.0

2.0

4.0

6.0

8.0

0

4

8

12

16

20

Deviatoric strain, ε_s [%]

(a)

M

1.35

1

S_r=1

Discontinuities

Yield curve of S_r=1

Deviatoric stress, q [kPa]

(b)

S_r=1

(c)

0.946 0.948 0.951 0.954 0.958 S_r= 0.964

0.956 0.958 0.960 0.963 0.966 0.970 0.975 0.981

0.980 0.982 0.984 0.988 0.992 0.997 1.000

S_r=1

Volumetric strain, ε_v [%]

Mean effective stress, p' [kPa]

(d)

S_r=1

Deviatoric strain, ε_s [%]

(a)

M

1.35

1

S_r=1

Yield curves

Deviatoric stress, q [kPa]

120

80

40

0

60

80

100

120

(b)

S_r=1

120

80

40

0

0

1

2

3

4

5

(c)

S_r=1

0.931

0.933

0.935

0.938

0.942

0.946

0.952

0.959

0.958

0.959

0.961

0.963

0.966

0.970

0.975

0.980

0.987

0.976

0.978

0.980

0.983

0.986

0.990

0.995

1.000

Volumetric strain, ε_v [%]

0.0

0.5

1.0

1.5

2.0

2.5

60

80

100

120

Mean effective stress, p' [kPa]

(d)

S_r=1

0.0

0.5

1.0

1.5

2.0

2.5

0

1

2

3

4

5

Deviatoric strain, ε_s [%]

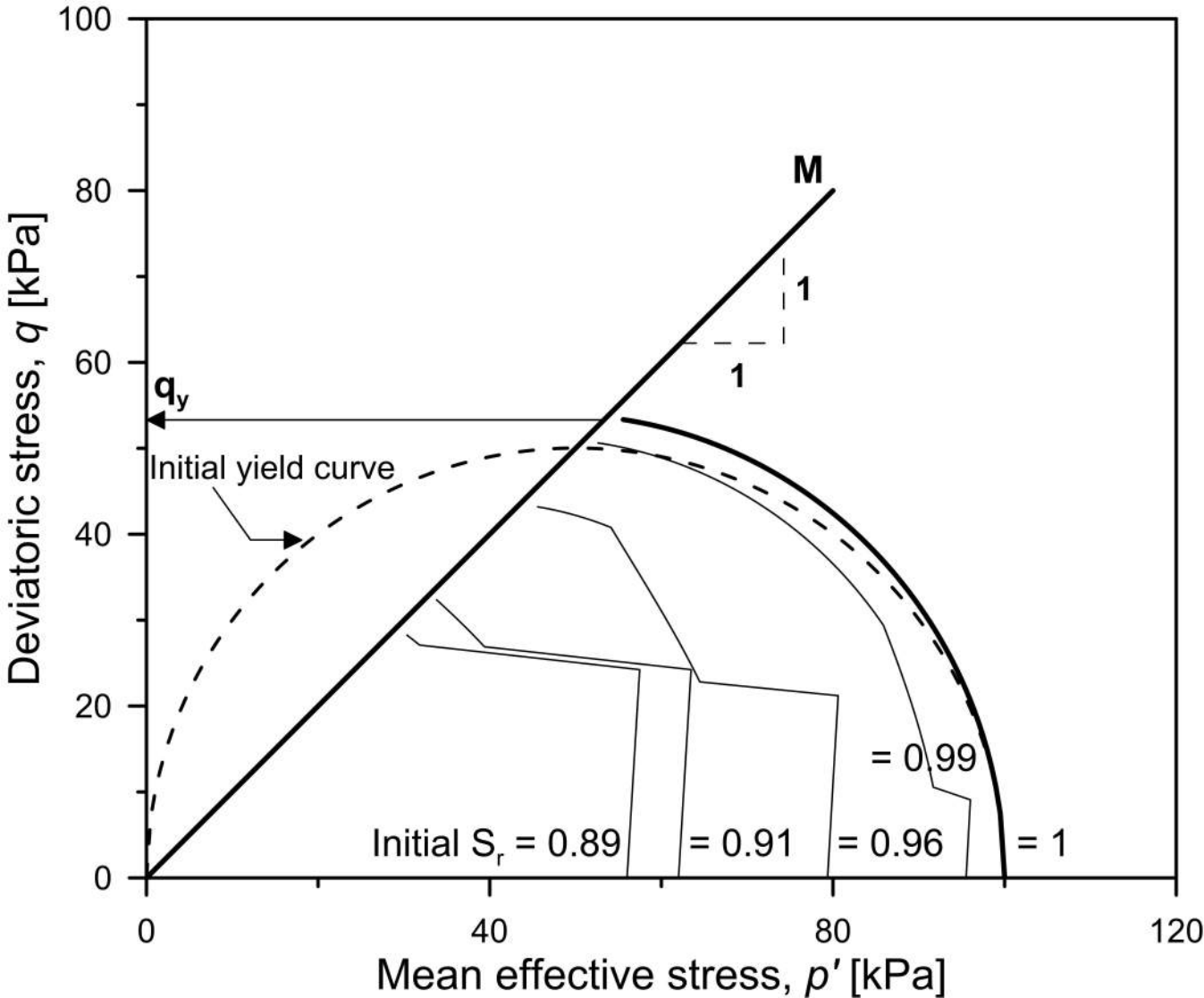
100
80
60
40
20
0
Deviatoric stress, q [kPa]
M
1
1
q_y
Initial yield curve
= 0.99
Initial S_r = 0.89
= 0.91
= 0.96
= 1
0
40
80
120
Mean effective stress, p′ [kPa]

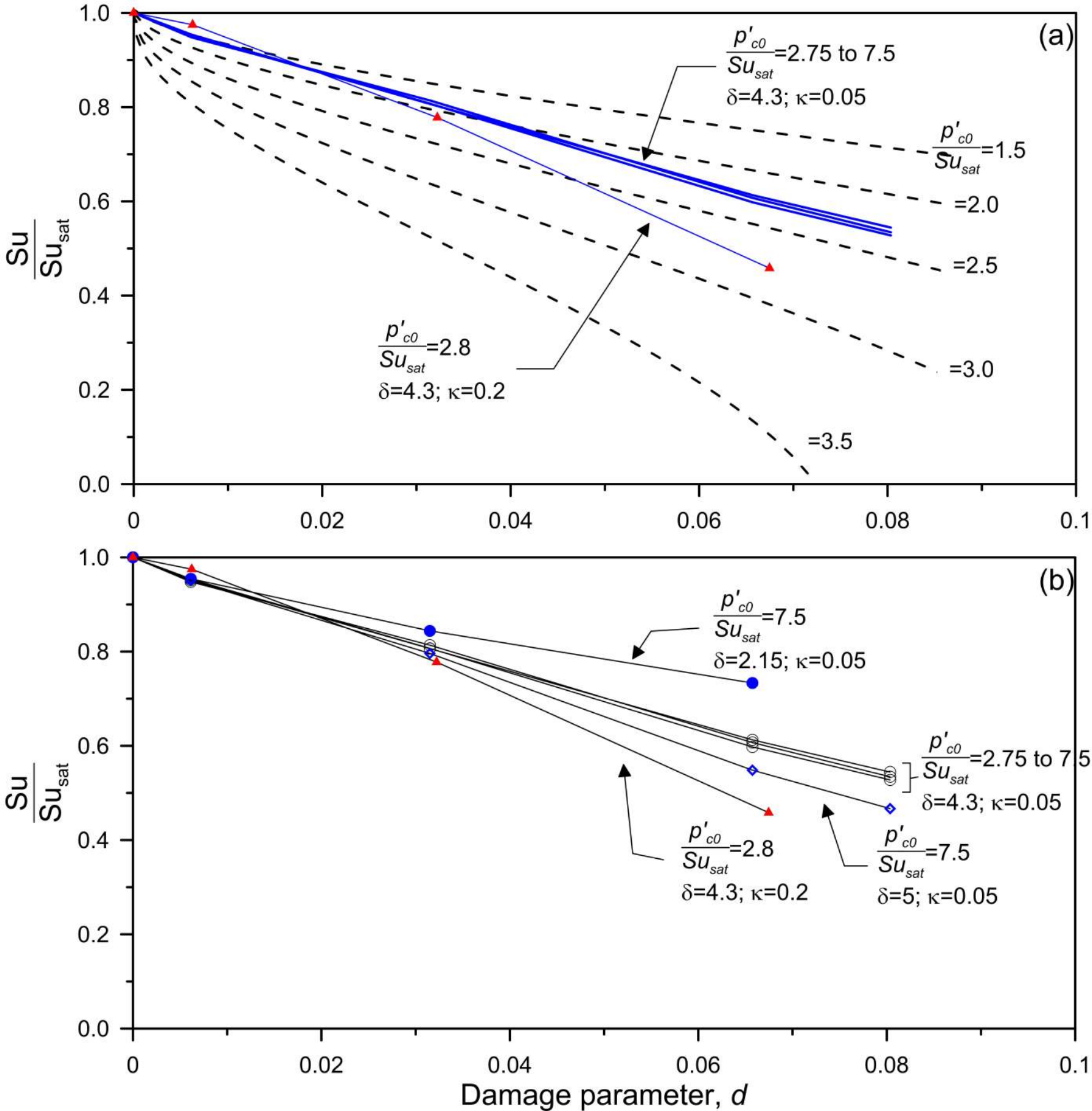
(a)
$\frac{p'_{c0}}{Su_{sat}}$=2.75 to 7.5
δ=4.3; κ=0.05
$\frac{p'_{c0}}{Su_{sat}}$=1.5
=2.0
=2.5
=3.0
=3.5
$\frac{p'_{c0}}{Su_{sat}}$=2.8
δ=4.3; κ=0.2
$\frac{Su}{Su_{sat}}$
(b)
$\frac{p'_{c0}}{Su_{sat}}$=7.5
δ=2.15; κ=0.05
$\frac{p'_{c0}}{Su_{sat}}$=2.75 to 7.5
δ=4.3; κ=0.05
$\frac{p'_{c0}}{Su_{sat}}$=2.8
δ=4.3; κ=0.2
$\frac{p'_{c0}}{Su_{sat}}$=7.5
δ=5; κ=0.05
$\frac{Su}{Su_{sat}}$
Damage parameter, d

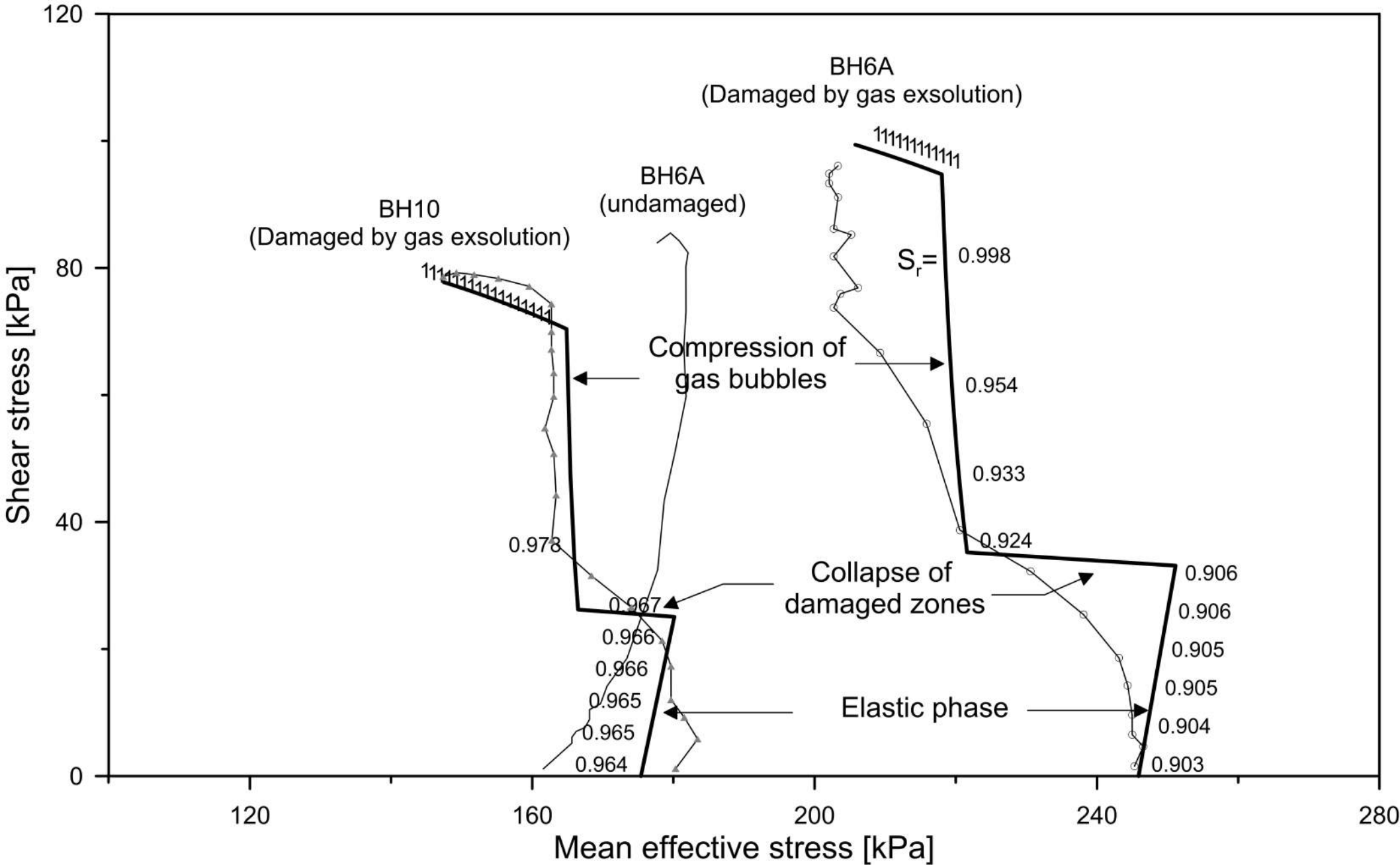
BH6A
(Damaged by gas exsolution)
BH6A
(undamaged)
BH10
(Damaged by gas exsolution)
S_r=
0.998
0.954
0.933
0.924
0.906
0.906
0.905
0.905
0.904
0.903
0.978
0.967
0.966
0.966
0.965
0.965
0.964
Compression of
gas bubbles
Collapse of
damaged zones
Elastic phase
Shear stress [kPa]
Mean effective stress [kPa]
0
40
80
120
120
160
200
240
280

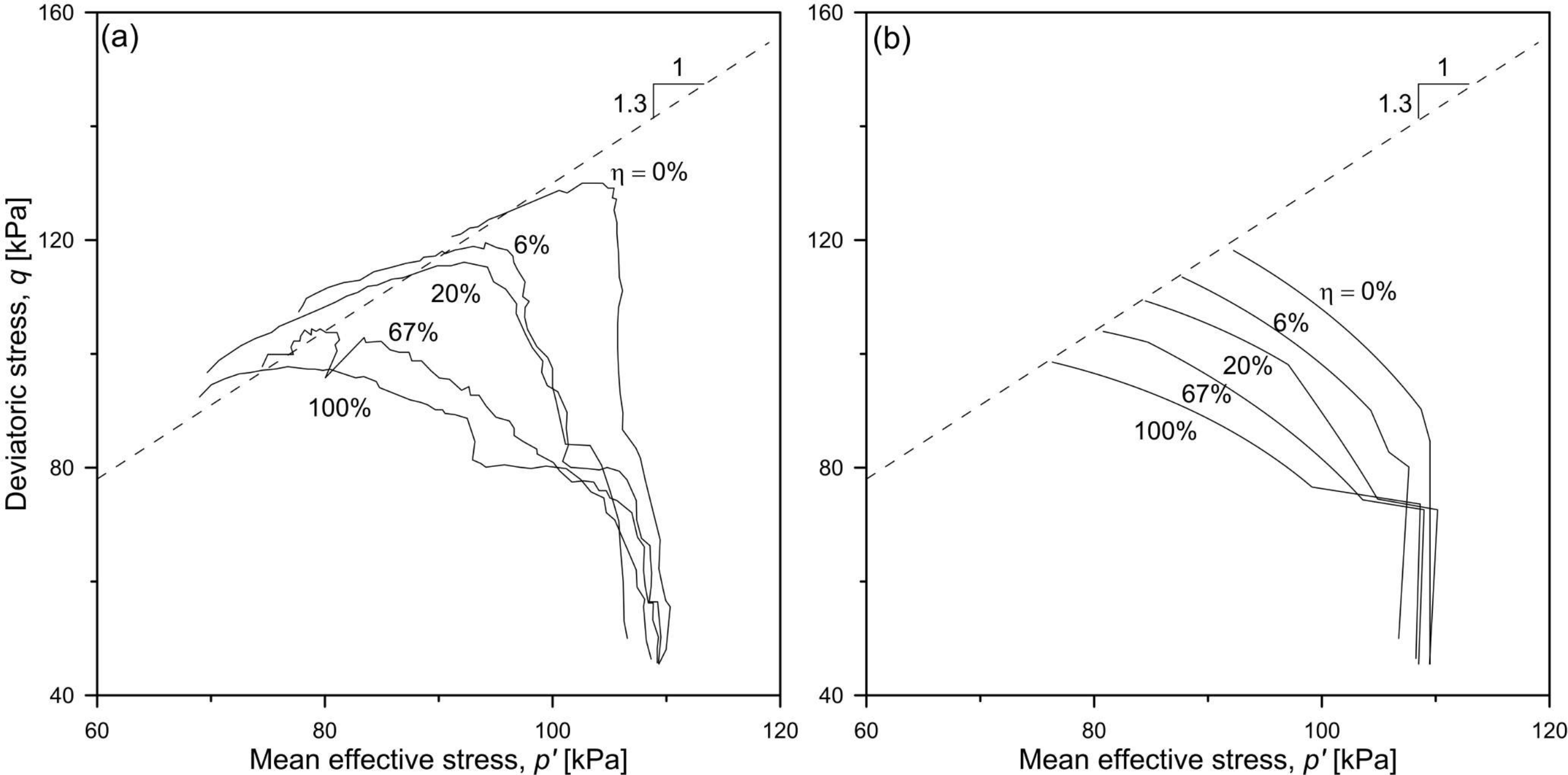
(a)
(b)
1
1.3
η = 0%
6%
20%
67%
100%
Deviatoric stress, q [kPa]
Mean effective stress, p′ [kPa]
160
120
80
40
60
80
100
120

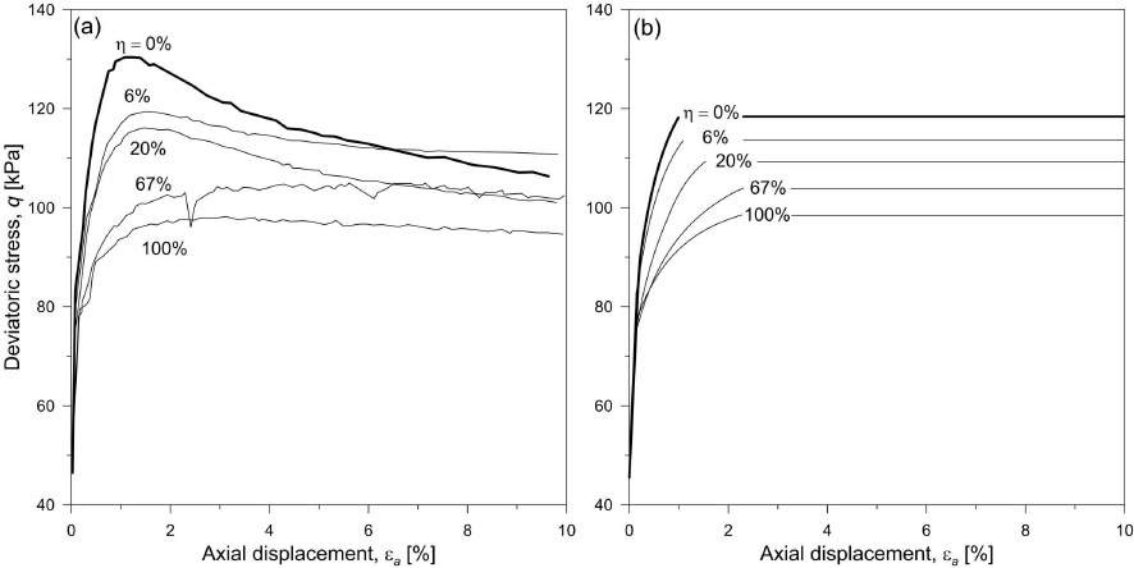
(a)
η = 0%
6%
20%
67%
100%
Deviatoric stress, q [kPa]
Axial displacement, ε_a [%]
(b)
η = 0%
6%
20%
67%
100%
Axial displacement, ε_a [%]

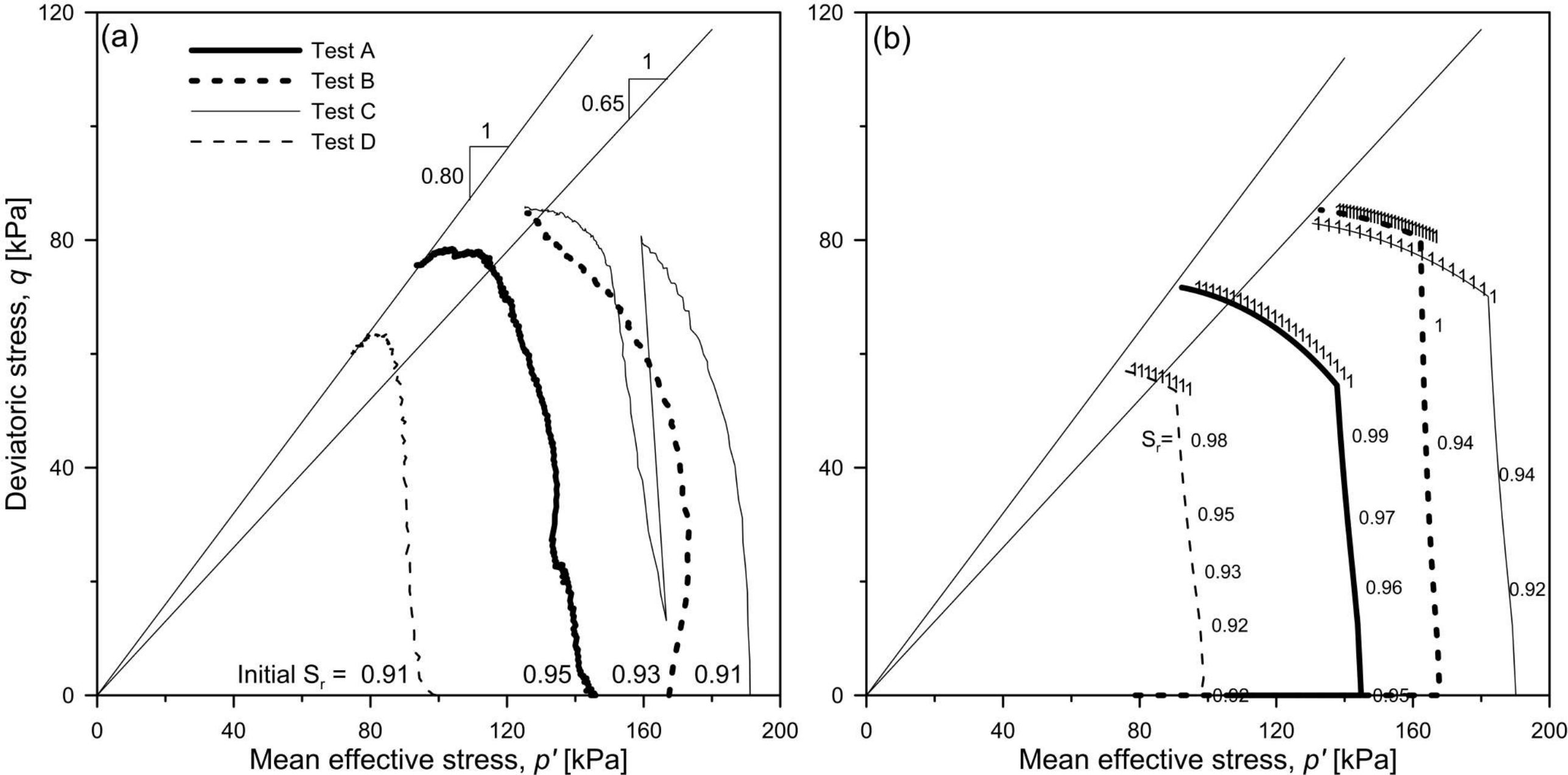
(a)
Test A
Test B
Test C
Test D
1
0.80
1
0.65
Initial S_r = 0.91
0.95
0.93
0.91
Deviatoric stress, q [kPa]
Mean effective stress, p' [kPa]
0
40
80
120
160
200
(b)
S_r =
0.98
0.95
0.93
0.92
0.99
0.97
0.96
0.94
0.92
1